

Flow Structures in the Tip Region for a Transonic Compressor Rotor

Juan Du

e-mail: dujuan111@gmail.com

Feng Lin

Jingyi Chen

Chaoqun Nie

Key Laboratory of Advanced Energy and Power,
Institute of Engineering Thermophysics,
Chinese Academy of Sciences,
Beijing 100190, China

Christoph Biela

Technische Universität Darmstadt
Petersenstrasse 30, 64287,
Darmstadt, Germany

Numerical simulations are carried out to investigate flow structures in the tip region for an axial transonic rotor, with careful comparisons with the experimental results. The calculated performance curve and two-dimensional (2D) flow structures observed at casing, such as the shock wave, the expansion wave around the leading edge, and the tip leakage flow at peak efficiency and near-stall points, are all captured by simulation results, which agree with the experimental data well. An in-depth analysis of three-dimensional flow structures reveals three features: (1) there exists an interface between the incoming main flow and the tip leakage flow, (2) in this rotor the tip leakage flows along the blade chord can be divided into at least two parts according to the blade loading distribution, and (3) each part plays a different role on the stall inception mechanism in the leakage flow dominated region. A model of three-dimensional flow structures of tip leakage flow is thus proposed accordingly. In the second half of this paper, the unsteady features of the tip leakage flows, which emerge at the operating points close to stall, are presented and validated with experiment observations. The numerical results in the rotor relative reference frame are first converted to the casing absolute reference frame before compared with the measurements in experiments. It is found that the main frequency components of simulation at absolute reference frame match well with those measured in the experiments. The mechanism of the unsteadiness and its significance to stability enhancement design are then discussed based on the details of the flow field obtained through numerical simulations. [DOI: 10.1115/1.4006779]

1 Introduction

The importance of flows in the tip region for axial compressors, especially modern transonic rotors, is well recognized in the gas turbine community. In addition to the fact that nearly 1/3 of the losses in rotors is contributed by the flow in the tip region [1], recent research results [2,3] suggested the tip leakage flow (TLF) and its interaction with the incoming main flow be responsible for spike-type stall precursor and rotating stall inception. Experimental and numerical efforts, in which the mechanism for effective control measures such as tip injection, casing treatments, etc. for compressor stability improvement are studied, also demonstrated the close relationship of TLF with the rotating stall in compressors [4–7]. All of these made the research of TLF a widely concerned topic of compressor aerodynamics in recent years.

Despite many efforts and impressive results, however, the roles that the TLF plays in stall precursor origination, especially those observed in transonic compressor rotors, are still unclear and even confusing, partially due to the isolation between experiments and computations. The observed phenomena in either experiments or computations are often interpreted from different viewpoints by different authors. In this paper, the two research groups, a computation group of CAS and an experimental group of TUD, Germany, are working closely to minimize the problems due to the aforementioned isolation.

The rotor under research in this paper is the Darmstadt Rotor 1, which is a transonic rotor of a single-stage transonic compressor rig at Technische Universität Darmstadt. The experimental results were published by the Darmstadt group, e.g., 2006 and 2008 [8,9]. Hah of NASA published his CFD results at the same time [10,11]. While the results were very impressive, especially on the unsteady features of TLF, they also indicate that the complexity of the TLF

in this rotor (as well as all transonic rotors in general) desires more efforts to dig out more complete flow images in the tip region.

In this paper, with a hope to clarify the details of TLF structure and evolved its unsteadiness, two research objectives are set up: (1) to unfold the flow structures at the rotor tip region, and (2) to characterize and validate the unsteady features of the self-induced unsteadiness found in near stall operating conditions. To the former, historically, Adamczyk et al. [12] illustrated the flow structure at the rotor tip region after examining the rollup of the tip leakage vortex, the shock wave, and the shock/vortex interaction in a transonic fan rotor. According to the result, stall happens when the low-velocity interaction region spills out of the blade passage when the incoming mass flow rate decreases to the stall limit. Puterbaugh and Brendel [13] further proposed a 2D model to describe the clearance flow-shock interaction in a transonic compressor rotor. In this paper we will extend Adamczyk and Puterbaugh's research and propose a new schematic of the flow structures by providing more detail in flow fields, especially those within the low velocity region, after completing a thorough study on the rotor tip clearance flow.

The unsteady characteristics are also the focus of this paper. Bergner et al. [8] and Hah et al. [10] experimentally and numerically investigated the same rotor, respectively. The oscillation in tip leakage flow was attributed to an induced vortex and the shock-vortex interaction. In 2008, new experimental results by Biela et al. [9] demonstrated that the unsteadiness of the flow in the tip region is mainly caused by tip leakage vortex oscillation, and that the rotating disturbance induces a frequency excitation band centered around 50% blade passing frequency (BPF) at both wall and stator leading edge instrumentation when operating the compressor close to the stability limit. In this paper, using an unsteady Reynolds averaged Navier-Stokes solver, we find and validate with experimental results that when the rotor operates at near stall, the tip leakage flow will produce a kind of unsteadiness named self-induced unsteadiness due to the dynamic interaction

Contributed by the International Gas Turbine Institute (IGTI) of ASME for publication in the JOURNAL OF TURBOMACHINERY. Manuscript received March 14, 2012; final manuscript received April 11, 2012; published online March 25, 2013. Editor: David Wisler.

Table 1 Test parameters at design conditions

Pressure ratio	1.5
Corrected mass flow rate	16 kg/s
Corrected tip speed	398 m/s
Rel. rotor inlet Mach number at tip	1.35
Rel. rotor inlet Mach number at hub	0.7
Shaft speed	20,000 rpm
Tip diameter	0.38 m
Inlet hub to tip ratio	0.51
Mean aspect ratio	0.94
Axial chord	41.26 mm
Rotor chord length at blade tip	94 mm
Relative tip gap (% of chord length)	1.7%
Solidity (hub/mid/tip)	1.9/1.5/1.2
Number of rotor blades	16
Number of stator blades	29

between the TLF and the incoming main flow [14]. We also propose that in order to make sensible comparison between numerical simulation in the rotor relative reference frame and the experimental casing absolute pressure measurements in the absolute reference frame, data conversions between these two coordinates are necessary.

This paper is organized as following. After Sec. 2, a brief introduction to the computational scheme and the experimental setup, the general flow structure in the rotor tip region is studied throughout in Sec. 3. The unsteady features are presented and discussed in Sec. 4, followed by a short list of conclusions in Sec. 5.

2 Experimental Setup and Numerical Method

2.1 Experimental Setup. A basic overview of the complete test setup at the Institute of Gas Turbines and Aerospace Propulsion at TUD, Germany is given by Schulze et al. [15]. The compressor stage under investigation in this study is the front stage of a high-pressure compressor in a modern commercial turbofan. Details of instrumentation, postprocessing, and measurement uncertainties are given by Bergner and Hennecke [16]. Unsteady static pressure at the casing was measured simultaneously with 14 axial equally distributed piezoelectric relative static pressure probes, which are placed at the casing above the rotor. The locations of these probes are displayed by Biela et al. [9].

The investigated titanium BLISK Darmstadt Rotor-1 is bladed with 16 radially stacked controlled diffusion airfoils profiles. Table 1 shows basic parameters of the compressor design.

2.2 Numerical Method. Single-passage simulations were performed by solving unsteady three-dimensional, Reynolds-averaged Navier–Stokes equations. Multipassage simulation results are not investigated in detail because the focus of this paper is the flow structure of tip leakage flow before the stall inception initiates, not the circumferential rotating disturbance induced by blade to blade interaction after stall inception occurs. A commercial solver package, FLUENT, was utilized for the present work. The solver is a three-dimensional, time-accurate code with implicit second-order scheme. Several numerical researches using this unsteady flow solver have been conducted for low-speed and high-speed compressor rotors [3,14,19], and the performance curves captured by computations matched with experiments well.

Turbulence is simulated by using Spalart–Allmaras (S–A) one-equation turbulence model. The mesh was refined in order to guarantee that y^+ at the first cell on the solid boundary is less than 5 to meet the resolution requirements because of the low-Reynolds description of the boundary layer in the Spalart–Allmaras model. Standard κ - ε turbulence model and standard wall function were also tested to ensure the precision of computation. It was demonstrated that prediction by applying the S–A turbulence model is better for this rotor.

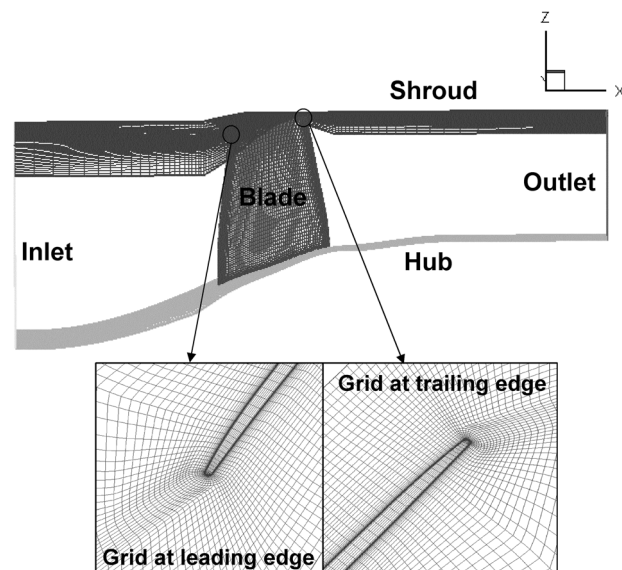
The computational domain and grid resolution including enlarged views of grid near blade tip leading edge and trailing edge are shown in Fig. 1. In order to ensure the computational results independent of grid distribution, mesh studies were conducted in steady simulations by coarsening and refining the mesh. Two grid systems, grid I and grid II are tested. The total number of grid I is approximately 0.52×10^6 and that of grid II is about 0.87×10^6 . It was proven that grid I is already sufficient for the computation and is a better compromise between accuracy and computational demands. Thus, grid I was used in the computation. The grid is a J-mesh, consisting of 79 nodes streamwise along the blade chord and 83 nodes in the spanwise direction including 20 nodes applied in the tip clearance region.

Total pressure, total temperature, and flow angles were given uniformly at the inlet boundary. Static pressure was specified with simple radial equilibrium law at the outlet. Nonslip and adiabatic conditions were imposed on all solid walls. For the time-accurate investigations, the physical time of each time step is 4.6875×10^{-6} s and 20 inner iterations of each time step were calculated.

3 General Flow Structure

The flows at the tip region are complicated by three typical flow elements, the tip clearance vortex, the shock, and their interaction. The model shown in [13] described the structural relation among these flow elements. In this section we will extend this model by providing three-dimensional (3D) details in these flows. After making the comparison of the compressor performance curve between CFD and the experiment, which can be considered a validation in one dimension, we presents the two-dimensional flow structures of TLF by observing the casing static pressure and relative Mach number contours. Then we analyze the three-dimensional flow structures with various three-dimensional plots, demonstrating the existence of an interface between the incoming main flow and the tip leakage flow. At last, the streamlines released at different parts along the tip chord are examined to further discover the three-dimensional flow structure of TLF and its link with flow loss and rotating stall. These analyses result in an illustration that shows the complex 3D flow structure at the tip region.

3.1 Compressor Performance Curve. Total pressure ratio and adiabatic efficiency performance curves at design rotor speed are presented in Figs. 2 and 3. The operating points marked with

**Fig. 1** Computational zone for single blade passage

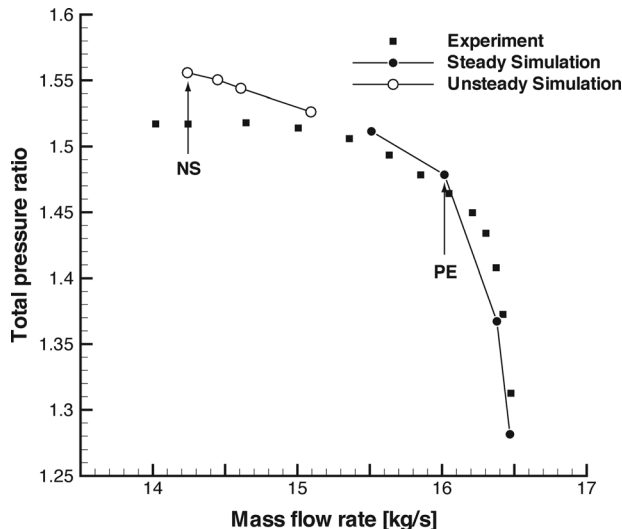


Fig. 2 Calculated and experimental total pressure ratio performance curve at design rotor speed

solid circles mean the flow fields at these operating points are steady, while the hollow circles are unsteady operating points. The flow fields in the tip region oscillate with a specific frequency at these unsteady operating points. PE and NS are the operating conditions near peak efficiency and near stall, respectively. The total pressure ratio curve predicted by numerical simulation is very slightly (<2.5%) above the experimental results. The predicted efficiency shown in Fig. 3 is on average roughly 5% above the experimental values. The reason for the discrepancy is likely to be that the experimental data is for one stage, while the numerical simulation was conducted for the rotor only. The fact that the discrepancies at near stall points are larger than those of peak efficiency points may be due to that the simulation at small mass flow rates underestimates the losses. The calculated mass flow rate of stall limit is 1.7% higher than the experimental values. These results suggest that the numerical scheme that we used throughout this paper captures the overall performance reasonably well.

3.2 Two-Dimensional Flow Structures. The flow structures in transonic rotor tip regions had been analyzed by many researchers [8–14]. According to the model proposed by Puterbaugh and

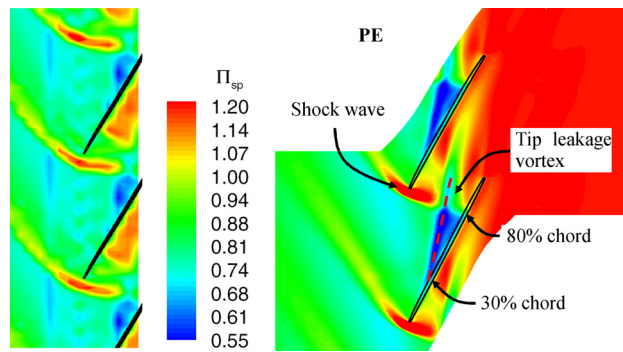


Fig. 4 Calculated and experimental static pressure contours at casing at point PE

Brendel [13], the tip leakage flow creates a tip leakage vortex, which soon intersects with the leading edge shock. Whether the shock is attached or detached depends on operating points. The vortex core is enlarged due to the reversed pressure gradient posed by the shock wave, creating a low velocity shock/vortex interaction region. In some rotors, the reserved pressure gradient is so large that the vortex breaks down. This region is referred to as blockage due to leakage flows by many papers. This understanding of flow structure can be confirmed in Figs. 4–6, in which the casing pressure and the relative Mach number contours for both PE and NS operating points are displayed.

Figures 4 and 5 show the calculated and experimental static pressure contours at casing at point PE and NS, respectively. Note that the simulation is done in the rotor reference frame. The experimental results were processed using phase-locking techniques to lock the same blade passage every rotor revolution and take the average over a number of revolutions to obtain steady pressure contours in the rotor reference frame. At peak efficiency, the static pressure distribution at casing in Fig. 4 and the Mach number contours in Fig. 6(a) show that the shock wave around the leading edge is detached, and the low-pressure slot marked with red dash line, which represents the trajectory of tip leakage vortex, is initiated at about 30% chord from the leading edge. The vortex trajectory extends streamwise through the blade passage, while intersecting with the shock at about 80% chord location. After the interaction there is a jump in casing static pressure, which clearly is due to the shock effect. All these match with the experiments very well.

When the compressor rotor runs at an operating point near stall, numerical simulation shows that the flow becomes unsteady and gets more complicated. In experiments the measured casing pressure data can be processed in three ways, the phase-locked mean

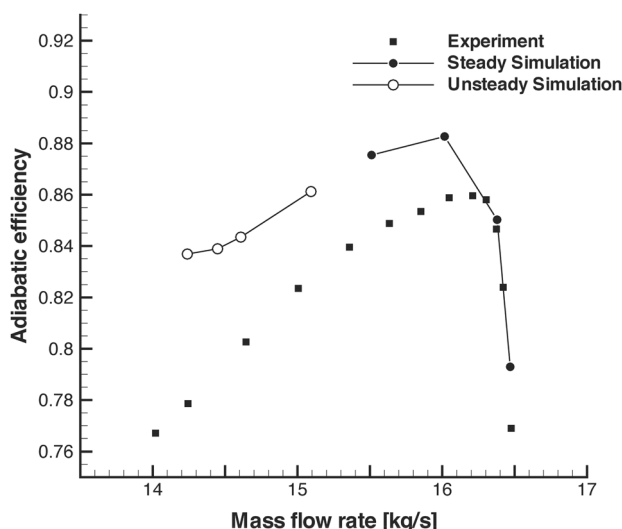


Fig. 3 Calculated and experimental adiabatic efficiency performance curve at design rotor speed

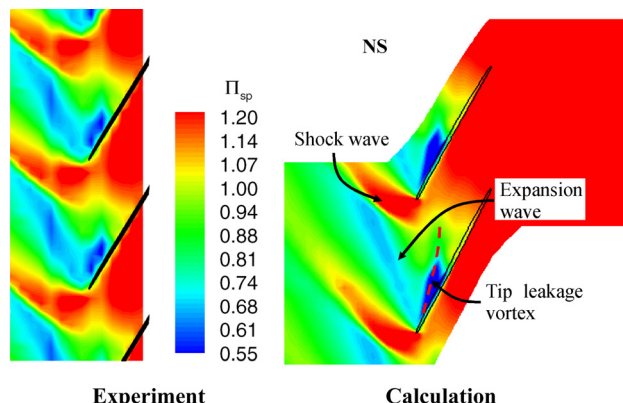


Fig. 5 Calculated and experimental static pressure contours at casing at point NS

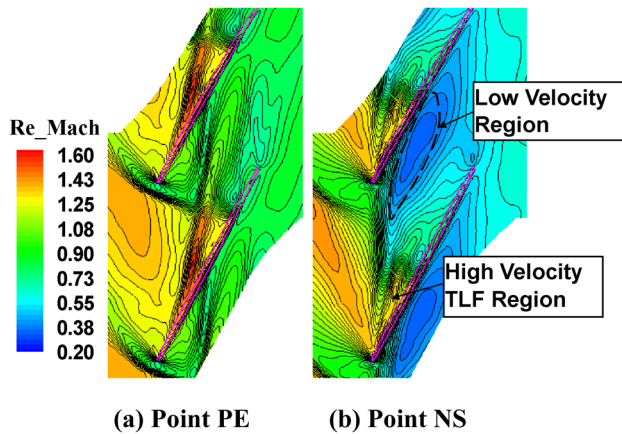


Fig. 6 Relative Mach number contours at 99% span, a plane at the middle of the tip clearance, at point PE and NS

contours, the standard deviation of pressure contours, and frequency spectrum contours. The phase-locked mean casing pressure contours are as depicted in Fig. 5. The other two contours will be analyzed in a later section. Compared to steady results in Fig. 4, the shock wave moves forward to the leading edge of the blade as the mass flow rate decreases, as well as the trajectory of the tip leakage vortex. After the detached shock wave, there is an expansion wave around the leading edge (see also Fig. 6(b)). All these flow structures existing at both design and near-stall operating conditions are captured by numerical results. Moreover, the values of the static pressure by simulation match with the experiments reasonably well.

Figure 6 presents the relative Mach number distribution at points PE and NS. It is a very good demonstration of Puterbaugh's model, especially the one for the near stall point. Note the relative Mach contours in Fig. 6(b) are time averaged. The same as in the Puterbaugh's model, the large low Mach area adjacent to the blade pressure side is the low-velocity region that was believed to be caused by the shock/vortex interaction. However, later in this paper we will show that this region, as well as the entire region that is dominated by the tip leakage flows, contains rich dynamics that desires in-depth three-dimensional analysis.

3.3 Three-Dimensional Analysis of Flow Structures

3.3.1 Main/TLF Interface. Figures 4–6 clearly show that the incoming main flow produces the shock wave, as well as the tip leakage flow generates the tip leakage vortex. However, what is not very clearly shown is the interface between these two flows. In recent years the existence of the interface between the main through flow and the tip leakage flow was found by Vo et al. [2] and verified by many others [14,17]. In order to clearly show the interface, several parameters can be used to distinguish the region of tip leakage flow from that of the main flow, such as entropy, relative total pressure, axial shear stress at casing, etc. In Fig. 7, relative total pressure contours in 3D for the operating points PE and NS are depicted to identify the region of influence by tip leakage flows, because the relative total pressure of the region dominated by the leakage flows is much lower. Note that in Fig. 7(b) the flow is unsteady, so the 3D relative total pressure contours are plotted for a time instant, not the time-averaged one due to technical difficulties in time averaging all the data on the nodes that fulfill the 3D volumes. But it is proven that the flows in all other time instants are qualitatively the same. In Fig. 7 the black line symbolizes the location of the interface between the incoming flow and tip leakage flow, before which the flow is dominated by the incoming flow, yet behind which the region is mainly influenced by tip leakage flow. The dashed line is the trajectory of the tip leakage vortex core.

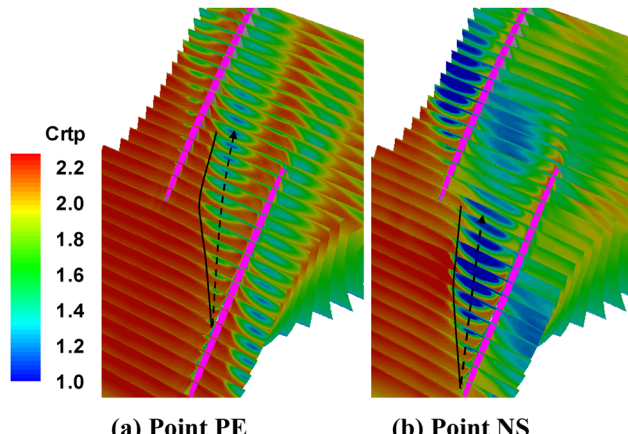


Fig. 7 Three-dimensional relative total pressure contours at point PE and NS, showing the existence of the region dominated by tip leakage flow and its interface with the main flow

A direct comparison between Figs. 7(a) and 7(b) can be made by visual observation. It can be seen that the interface at point NS is located much closer to the leading edge than that at point PE. Meanwhile, it can be shown that the region of influence by the tip leakage flow at point NS penetrates much deeper spanwise than at point PE. According to Vo's criteria, such an interface may cause spike-type stall inception if it spills out of the blade leading edge.

3.3.2 3D Flow Structures. Now we turn our attention to the 3D flow structures, especially its implication to stall. In order to unveil 3D flow structures, it is necessary to examine closely (1) how the interface is formed, (2) the role of the shock, and (3) the behavior of tip leakage flow behind the interface. We find out that one of the best ways to illustrate these related flow structures is to use streamlines. We release particles in the middle of the tip gap and along the tip chord, and then follow them through the 3D flow

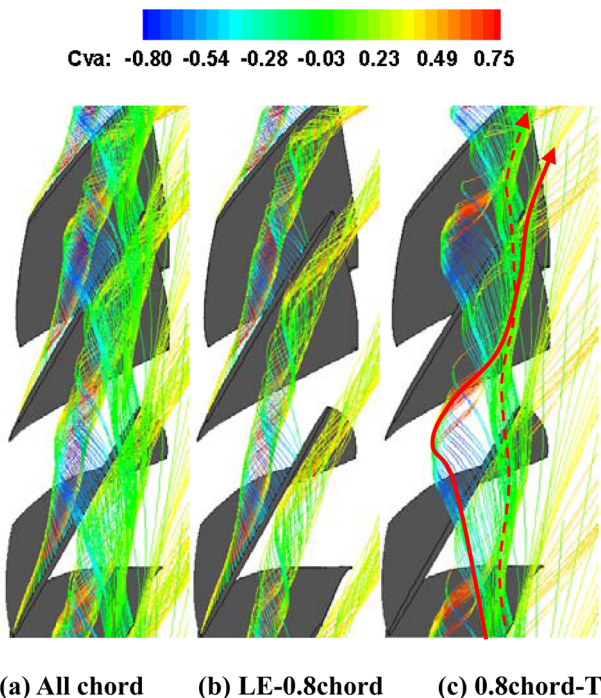
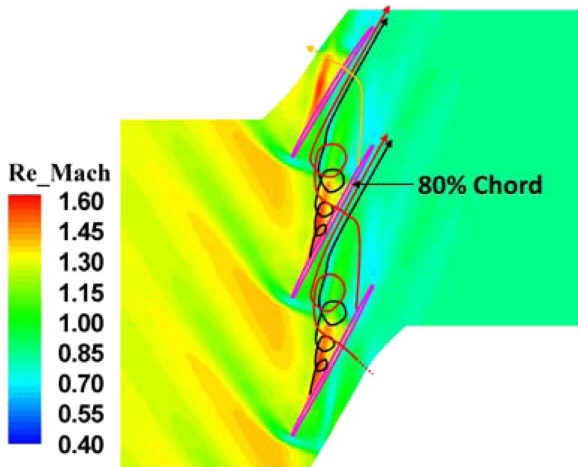
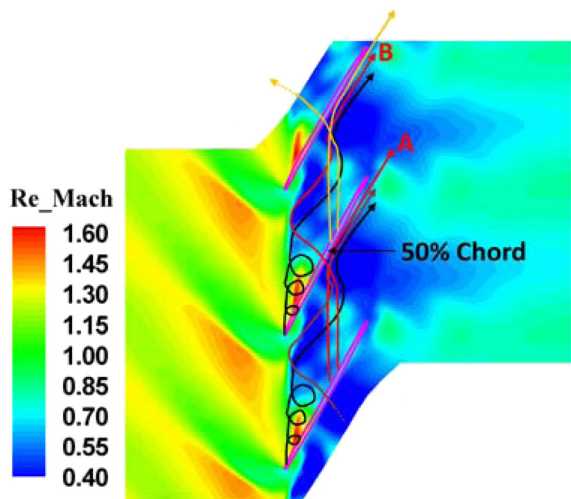


Fig. 8 The streamlines released in tip region at point PE. The colors are axial velocity component. (a) The streamlines all over the entire chord. (b) The streamlines over the first 80% chord. (c) The streamlines over the last 20% chord.



(a) Point PE



(b) Point NS

Fig. 9 Illustration of tip leakage flows and their evolutions

field. The colors on those streamlines can be used to illustrate the values of various parameters, such as axial velocity component, static pressure, etc. This method has been used by Hah et al. [11] when studying this very same rotor, proven to be effective. We start with the case with large flow rate and far away from stall. Figure 8 depicts the streamlines for steady flows at point PE. The streamlines across three blade passages are generated by duplicating the streamlines from the calculated blade passage. The colors are the axial velocity component. As demonstrated in this figure, the streamlines all over the entire chord length is clearly divided into two segments. Over the first 80% chord from the leading edge, the tip leakage flow is completely rolled into the tip leakage vortex, while over the rest 20% chord, the tip leakage flow is obviously more complicated. For clarifying these two different tip leakage flows, the streamlines in Fig. 8(a) are replotted in Figs. 8(b) and 8(c) separately. In Fig. 8(b) the streamlines from the first 80% chord are plotted alone, and one can see these lines clearly revolve into the tip leakage vortex, which then smoothly flows out of the blade passage. In Fig. 8(c), the situation is a bit complicated. The tip leakage flow over the last 20% chord does not roll into the tip vortex directly. Instead, they go across the blade passage and impinge the neighboring blade, where they are divided

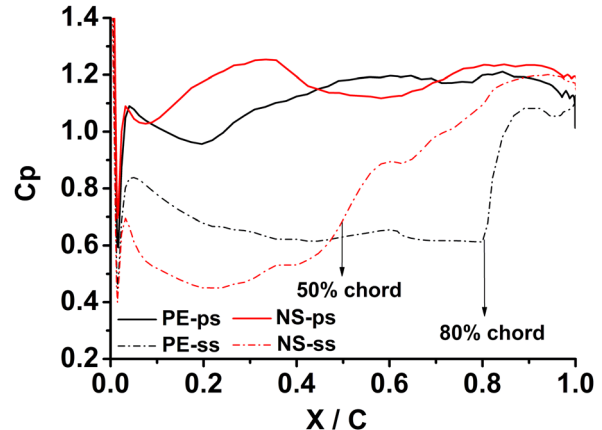


Fig. 10 Blade loading distribution at point PE and NS

further into two streams. If the flows strike the region within the first 80% chord (marked with a solid red line), they leak over the neighboring blade tip and roll into the vortex in the neighboring passage. If they strike the last 20% chord of the neighboring blade (marked with a dashed red line), they will then never roll into the vortex at all; they simply leak across the tips again and again, blade after blade. Similar flow structure was also reported in [11].

Figure 9(a) is a schematic that summarizes the flow structure at the peak efficiency point PE which is plotted on top of the relative Mach number contours at casing surface. One can see the location of 80% chord is indeed the point where the shock wave starts to influence the blade suction side (see also Fig. 5). This can also be confirmed by the blade loading as shown in Fig. 10. The pressure coefficient distribution over the blade at points PE and NS are plotted with a black and red line separately. As shown in that figure, the blade loading at point PE becomes flat after a sharp drop due to the shock wave at 80% chord. Meanwhile, the tip leakage vortex that is initiated by the first 80% chord of tip leakage flows goes downward and sinks away from the tip gap. The tip leakage flow in this later 20% chord thus has a chance to go across the blade passage without being absorbed into the vortex. However, if any part of these flows strikes the first 80% chord, secondary leakage happens and the secondary leakage flow is evolved into the tip leakage vortex.

At point NS the blade loading is shifted toward the leading edge, as shown in Fig. 10, so is the location of shock influence. The new location is approximately at 50% chord for one time instant. We then draw the streamlines divided in half, one for the first 50% chord, the rest for the other half. Figure 11 depicts the numerical simulations of the streamlines over the two different chord portions at one time instant, which is illustrated in Fig. 9(b). The flow patterns for the two different chord portions are quite different. The tip leakage flows over the first 50% chord roll up into the tip vortex and flow through the blade passage without impinging any blades. The flows in the other half are further divided into two parts, one between 50%–80% chord and the other from 80% chord to the trailing edge, marked as A and B symbolically on Fig. 11(c), respectively. Path A goes across the blade passage and impinges the neighboring blade without getting evolved into the tip leakage vortex, while path B goes along the same direction as path A at the beginning but leaks over the rotor tip the second time and eventually rolls into the tip leakage vortex in the neighboring blade passage. The reason for the further division of the tip leakage flows in the second half chord is not clear at this point, which deserves further investigation, especially with unsteady flow analysis. The flow structure and the role played by each part of the tip leakage at each time step are found to be qualitatively similar after checking the unsteady flow fields for each time instant. The static pressure distributions at two typical time instants are shown in Fig. 14 and will be discussed in Sec. 4.1.

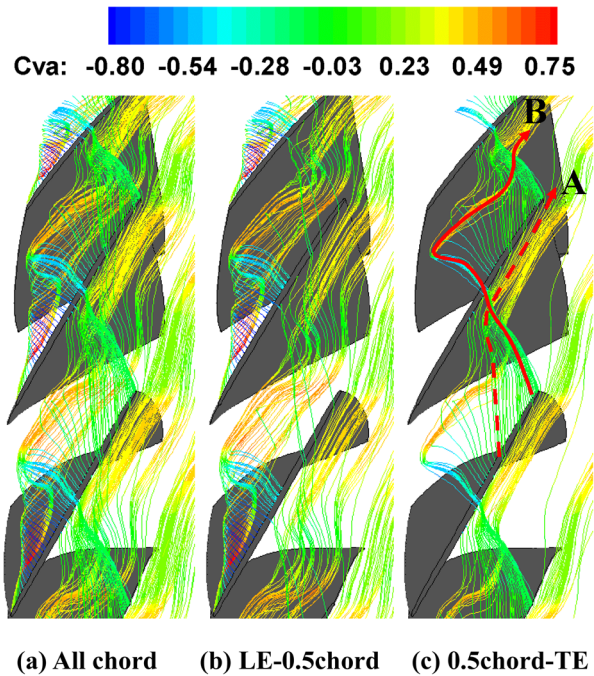


Fig. 11 The instantaneous streamlines released in tip region at the point NS at 45/40 T. The colors are axial velocity component. (a) The streamlines all over the entire chord. (b) The streamlines over the first 50% chord. (c) The streamlines over the last 50% chord.

3.4 Significances and the Discussion. In short, the 3D flow structure can be illustrated with a schematic as shown in Fig. 12. The above analysis implies that the roles that different portions of the tip leakage flows play in determining the location and orientation of the main/leakage flow interface can be quite different from each other. The first portion, i.e., flows from the leading edge to wherever the divided point, produces “strong” (meaning high speed, normal to blade camber line which in turn possesses large negative axial velocity component) tip leakage flows that interact with the incoming main flow and produce the strong tip leakage vortex. The second portion, i.e., flows from the divided point to the trailing edge, is attributed to the change of blade loading distribution along the chord. In this particular rotor under current study, the change comes from the shock wave. Such loading change can come from different causes in different rotors. At the peak efficiency point PE, the first portion of the tip leakage flow dictates the initial location and dominates the entire interface orientation going downstream. While at the near stall point NS, as

seen in Fig. 11 and illustrated in Fig. 9(b), the tip leakage flow over the first 50% chord governs the initial position of interface near the suction side, and the second portion of tip leakage flow interacts with the incoming flow near the pressure side of the neighboring blade shifting the interface upstream. As the rotor is closer and closer to stall, it can be expected that the divided point would move closer and closer to the leading edge, making the second portion leakage flow stronger and stronger, which in turn would more and more likely push the interface out of the blade passage. For this reason, even though the leakage momentum at this second portion can be smaller than that at the first portion, it still plays a key role in determining the location of interface near the pressure side of neighboring blade. According to the research by Vo et al. [2], the spillover of the interface is one of prerequisites for the occurrence of spike type stall inception.

4 Unsteady Flow Features

One of the flow features reported in the experiments of Darmstadt Rotor 1 is its unsteadiness [9]. According to the first picture in Fig. 13 of Ref. [9], the frequency spectra of the data collected by a probe at about 8% blade chord from the leading edge, we noticed that there are two fundamental unsteadiness found in the experimental results. At near stall, the spectrum consists of a broadband “noise” and a “hump” that was marked as “excitation @ NS,” both of which were not seen at the peak efficiency point. Since the turbulence in flows is typically broadband, the noise is considered as a consequence of turbulence within the blade passage. The reason for such strong turbulence at near stall condition is still unknown. One of such sources can be the shock/boundary layer/vortex interaction. We name this kind of unsteadiness as *turbulence unsteadiness*.

Since in numerical simulation it is one order more costly and difficult to resolve the turbulence in this complex rotor tip flows, we will center our computational focus on the hump. This hump extends from 2000 to 4000 Hz (or 0.375 to 0.75 BPF), containing multiple frequency components within it. This hump might be due to some sort of deterministic dynamics. As demonstrated later in this section, we capture this unsteadiness with our CFD simulation.

4.1 Unsteady Phenomenon. The unsteady simulations for this isolated rotor were run at the design rotating speed with various back pressures. Monitoring points along the whole blade chord are set near the blade tip to record the history of static pressure with time to estimate whether the flow field in the tip region fluctuates or not. As shown in Fig. 2, there are four operating points with unsteady tip clearance flow on the performance curve. Note that point NS is that with the highest back pressure before the iterative process diverges. The unsteady features of flow

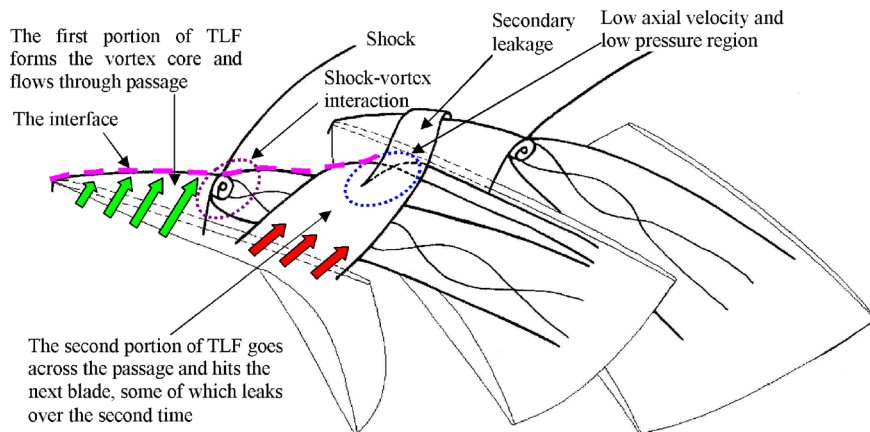


Fig. 12 The schematic of the 3D flow structures of tip leakage flows

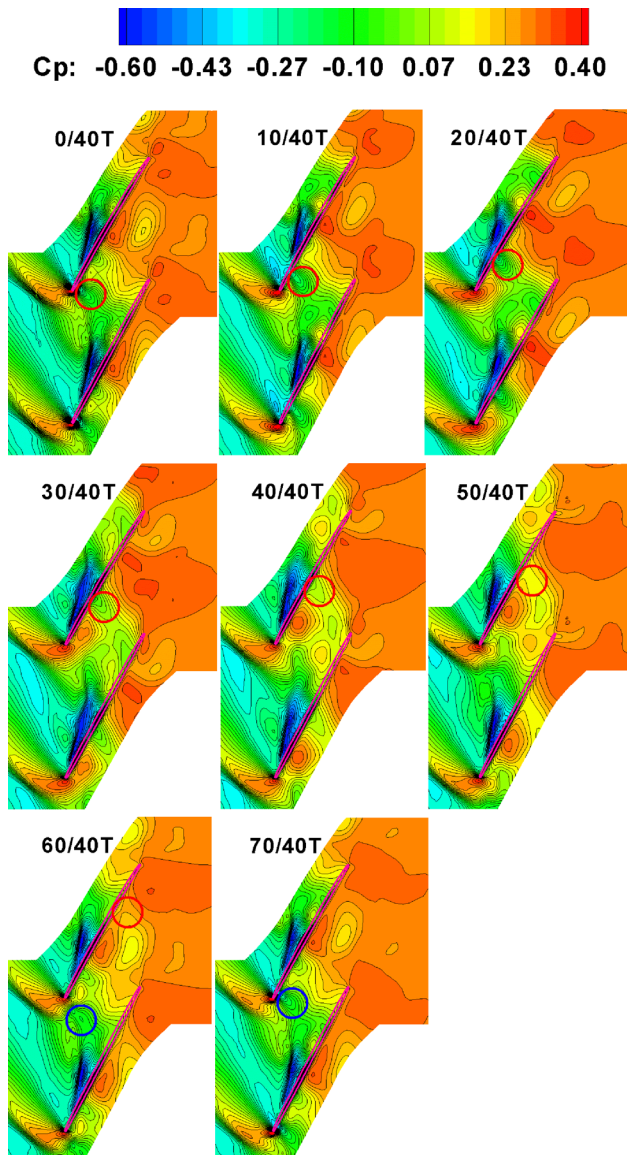


Fig. 13 Instantaneous static pressure contours at casing surface at eight time instants

structures in the tip region at this near stall case will be analyzed in this section.

Before examining the unsteady features of the flow structure in the tip region, we present the unsteady phenomenon of simulation by displaying eight images of static pressure contours at different time instants given in Fig. 13. The contours of static pressure coefficient (C_p) are used. According to the investigation by Inoue [18], the trajectory of the tip clearance vortex could be identified by the static pressure trough of the minimum pressure region. The abrupt change of static pressure can estimate the location of the shock wave. From 0/40 T to 50/40 T, a couple of local high-pressure and low-pressure spots are along the first half of chord on the pressure side. According to Ref. [14], the low-pressure spot is actually a part of the region influenced by the tip leakage flow, marked by a red circle in Fig. 13. The incoming main flow creates a high-pressure spot on the pressure side when it is blocked by the strong tip leakage flow. The high-pressure spot pushes the low-pressure spot to wash downstream the blade chord. At 60/40 T time instant, the new local low-pressure spot arrives at the pressure side when the tip leakage vortex impinges with the blade, and then a new local high-pressure spot appears because of incoming flow. As time moves forward, the new low-pressure spots marked

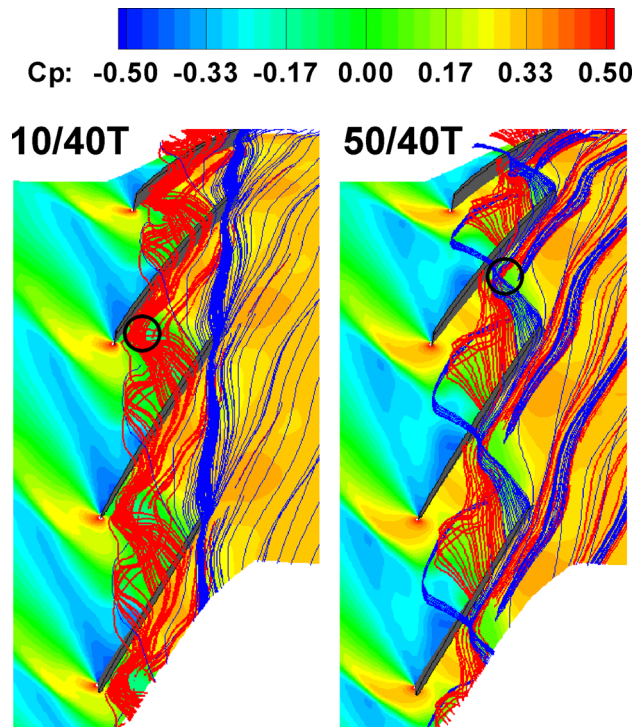


Fig. 14 Static pressure contours at 90% span and streamlines over the last half chord in the middle of the tip region at two different time instants

by a blue circle at 70/40 T replaces the location of the old one at 0/40 T time instant, the flow fields start next cycle. The mechanism of unsteadiness for rotor 1 is the same as that of self-induced unsteady tip leakage flow (UTLF). The reason for which we call it “self-induced” is that it is confined within one blade passage and caused by the tip leakage vortex impinging on the neighboring blade’s pressure side. Or, it is triggered by itself. It is a phenomenon we found in a low-speed rig of our own (both computationally and experimentally [5]) and in NASA Rotors 67 [14] and 37 [19] (CFD only).

This originating mechanism can be further refined with the understanding of the flow features in the tip region as presented in Sec. 3. As described in Sec. 3, it is the part of TLF over the second half chord that impinges the neighboring blade, creating a low-pressure spot on the pressure side, and forms the second segment of the interface across the blade passage. Figure 14 demonstrates that this is exactly the case in which two different time instants of the unsteady process were snapshot. In Fig. 14 the red streamlines are released from 50% chord to 80% chord in the middle of the tip region, while the blue ones are the streamlines over the last 20% chord. The black circle symbolizes the low-pressure spot on the static pressure contours at the 90% span surface. One can see that at each time instant the low-pressure spot coincides with the impingement location of the tip leakage flow nicely.

4.2 Location of the Unsteadiness. To view the location of the unsteadiness within the blade passage, we present the contours of the standard deviation (STD) of static pressure distribution on pressure and suction side surfaces at near stall point. The value of the STD of static pressure can be used to demonstrate the distribution of oscillating strength. Figure 15 gives the whole view about the oscillating strength distribution along blade height. The high static pressure standard deviation regions are concentrated on the tip region for both surfaces. The oscillation on the pressure side is much stronger than that on the suction side.

Figure 16 presents the comparison of STD of static pressure distribution at casing between CFD and experiment. Note that the

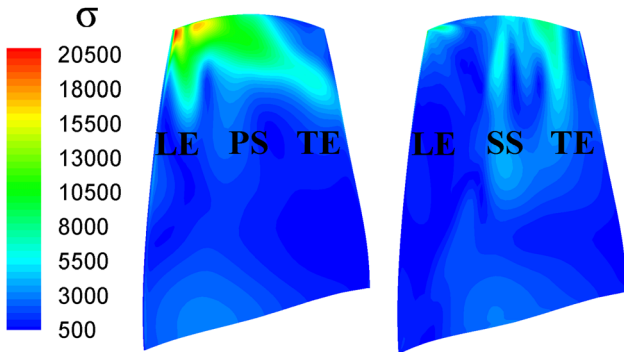


Fig. 15 Static pressure standard deviation contours on pressure side and suction side surfaces at point near stall

experimental result is obtained by first phase locking the same rotor blade passage for a number of rotor revolutions, and then calculating the mean and STD based on the phase-locked data. By doing so, the data on the casing absolute frame can be viewed in the rotor relative frame, which is thus comparable with the numerical results in the rotor relative frame. From Fig. 16 it can be observed that the STD distribution calculated by CFD matches the experimental results reasonably well. The higher overall level of the experimental data is not entirely caused by aerodynamic effects of the passage flow but as well by the instrumentation or inflow conditions. There are two highly fluctuating regions in the blade passage at casing. The strongest fluctuation region marked with a black oval is located near the pressure side of the blade where the trajectory of the tip leakage vortex impinges with the blade most often. The second strongest region is the region of the tip leakage vortex and the interaction between the vortex with shock wave, which is marked with a black dash oval.

4.3 Frequency Characteristics. The frequency characteristics are presented in both the rotor relative reference frame and the casing absolute reference frame. First, in the rotor reference frame, a total of 20 monitoring points are set and the locations of these points are indicated in Fig. 17. Half of these points are on the pressure side of the blade at 98% span, which are represented by “bp” with subscripts from 1 to 10. The other half are located in the flow field near the suction side of the blade, which are marked with “V”. Points V1 and V2 are set on the location of the shock wave to capture its oscillation. The monitoring points from V7 to V10 are along the trajectory of the tip leakage vortex. The time history of these points are recorded and the FFT analysis results for these data are given in Fig. 18, in which Fig. 18(a) is for bp1–bp10 and Fig. 18(b) is for V1–V10. There are two oscillating frequency components, one of which is 3056.68 Hz or 0.57 BPF. The other is 6218.76 Hz or 1.17 BPF. The dominating frequency component is 0.57 BPF. It also can be seen from Fig. 18(a) that the highest oscillating region on the pressure side is at around the 20% chord from the leading edge, and the main fluctuation region is confined within only 50% tip chord from the leading edge. Figure 18(b) indicates that the oscillation at the location of the shock wave is much weaker than that in the region of the tip leakage vortex. This implies that the shock wave alone is not the major cause of the unsteadiness. Note that the monitoring points are set in the relative reference frame, so this frequency is obtained in a relative coordinate frame on which the observer is moving with the rotating blade passage. Thus, the blade passing frequency and the rotor rotating frequency cannot be seen in FFT results of Fig. 18.

In order to compare the calculated frequency characteristics with those measured on the casing reference frame, the data sampling exactly as what is being done in the casing absolute reference frame is simulated. This is done by placing seven virtual monitoring points at the casing, at the same locations as those of

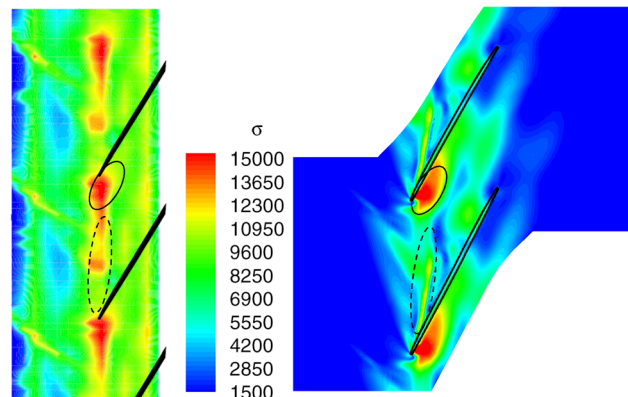


Fig. 16 Calculated and experimental standard deviation of static pressure distribution

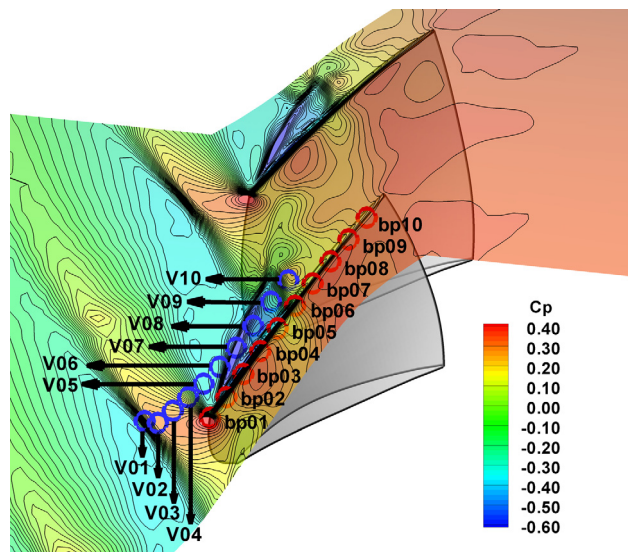
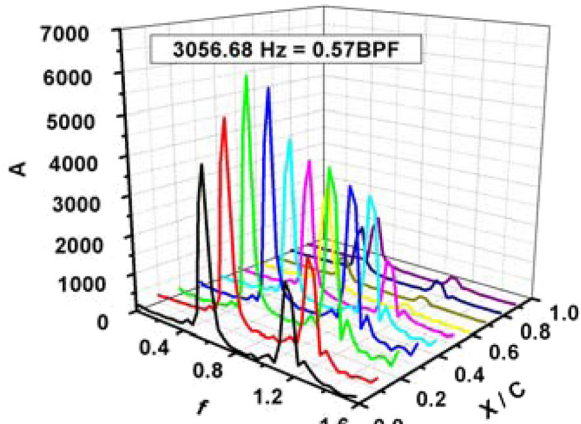


Fig. 17 Locations of monitoring points

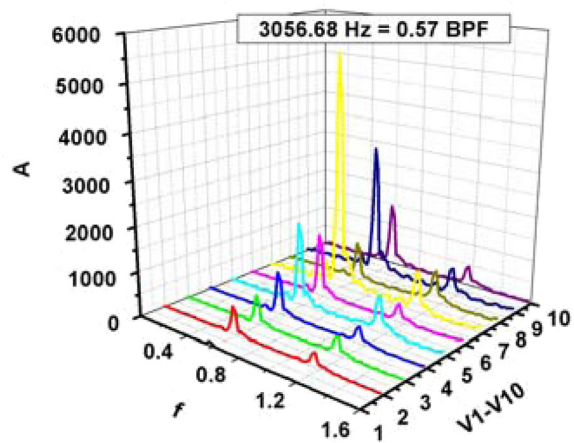
probes 08 to 14 in the experiment by Biela et al. [9], and then recording the static pressure readings as these virtual points move in a direction opposite to the rotor rotation, yet with the same speed of rotor rotation. Figure 19 illustrates this idea.

Note that in experiments the blade passages that sweep through each probe vary from time to time as the entire rotor rotates underneath the probes. In the current single passage simulation, we duplicate the identical blade passages to emulate the multipassage rotor. This will certainly causes discrepancies between experimental and calculated frequency, which is acquired from the pseudo data in the absolute reference frame. One of such discrepancies is that the numerical data acquired at casing cannot have frequency components related to rotor revolution, because all the blade passages that the probes sweep across are exactly identical, so that there is no way to see when the rotor rotates exactly one revolution. In contrast, in experiments the frequency components related to one rotor revolution may not only be caused by the blade-to-blade variation but also due to the mechanical vibration of the rotor itself.

Note that these virtual monitoring points are now in the absolute reference frame. Thus, the time history of static pressure recorded by these monitor points can reflect the effects of blade passing. The frequency spectrum of virtual probe 10 on the casing absolute reference frame is given in Fig. 20(a). As a comparison, the frequency spectrum of probe 10 at the same axial location



(a) bp1-bp10



(b)V1-V10

Fig. 18 Frequency and amplitude characteristics in tip region within relative reference frame

fixed on the rotor pressure side is given in Fig. 20(b). One can see that while there are only two fundamental frequency components in the rotor reference frame, the observer on the casing is observing a much more rich frequency spectrum. What is happening is that the two fundamental frequencies modulated with the blade passing frequency, generating more frequency components by combining these frequencies with addition/subtraction among them. Such frequency modulation is very important for both computationists and experimentalists to understand the observed phenomena correctly.

Place the frequency spectra for all the virtual probes together and a contour of frequency components can be produced, as shown in Fig. 21. Comparison can be made between the experimental results in Fig. 21(a) and the simulation results in Fig. 21(b). There are two frequency bands in Fig. 21(a), one ranging from roughly 2000 to 3800 Hz, the other from 4000 to 5000 Hz. Within the first frequency band, there are three peaks in Fig. 21(b), 2292, 3073, and 3854 Hz, among which the last peak is much smaller than the first two. We consider this a good match between the simulation and the experiments, given the fact that the experiment environment is much noisier, and thus it is common that a group peaks in the clean simulated data would correspond to a frequency band in experiments. The second good

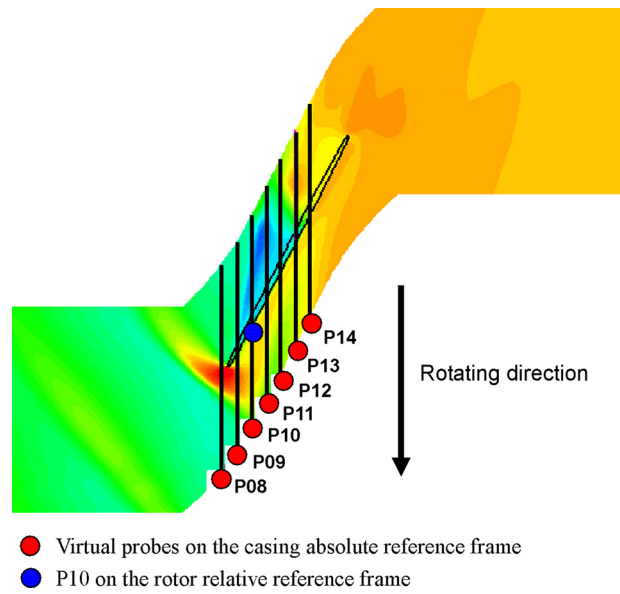
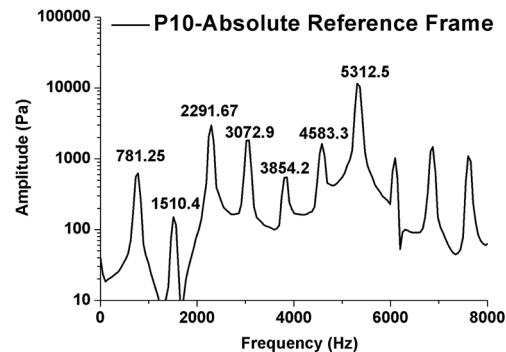
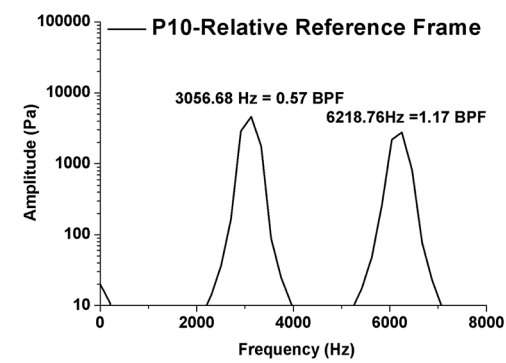


Fig. 19 The illustration of how to convert the calculated rotor reference frame data to the casing virtual probe data



(a) Spectrum on the casing absolute reference frame



(b) Spectrum on the rotor relative reference frame

Fig. 20 The comparison of frequency spectra on the casing absolute with the rotor relative reference frame

match is that the peak at 4583 Hz is almost centered at the frequency band of 4000–5000 Hz in experiments. In other words, we believe the two frequency bands in experiments all come from the same unsteady source, the self-induced unsteadiness of TLF.

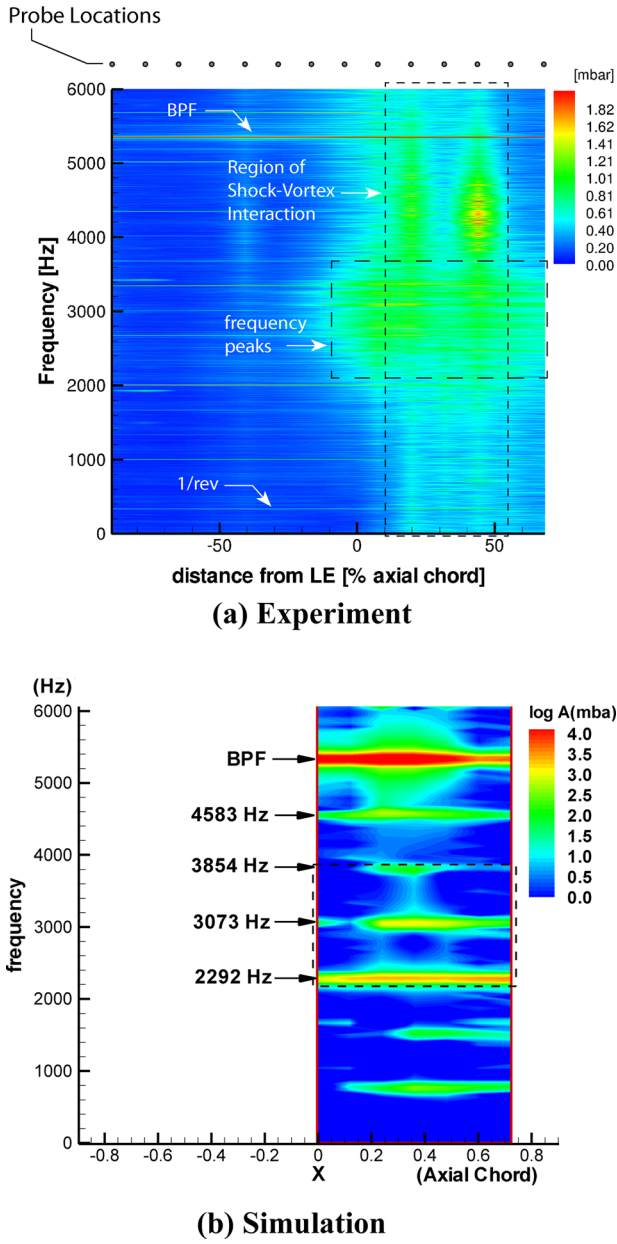


Fig. 21 Frequency of signals in absolute reference frame of experiment and simulation

Up to this point, the phenomenon and the characteristics of the self-induced unsteadiness are presented and compared with experimental results. The existence of such unsteadiness in this rotor is thus confirmed. Its mechanism was proposed by Du et al. [14], in which the origination of the self-induced unsteadiness can be attributed to the interactive dynamics between the incoming main flow and the tip leakage flow. It was shown that the location of the interface is determined by the momentum balance of the main flow and the tip leakage flow. Once the interface moves forward to some location close to the leading edge but before spillage, the influence of the tip leakage flow on the neighboring blade's pressure becomes strong enough to significantly change the blade loading, which in turn changes the tip leakage flow itself and creates oscillations.

5 Conclusions

In this paper the flow structures in the tip region of a transonic rotor are investigated numerically and experimentally. The two

major discoveries are: (i) The three-dimensional structures of TLF, and (ii) the unsteady characteristics of TLF, positively validated by experimental results. These are summarized in details as below.

1. The TLF along the blade chord can be divided into at least two parts according to the blade loading distribution. The first portion of the TLF interacts with the main flow and rolls up into a tip leakage vortex. The second portion of the TLF goes across the blade passage and impinges the neighboring blade's pressure side. The vortex core may be slowed down and enlarged once it interacts with the shock.
2. The spillage of the main/TLF interface is controlled by the combined action of the first and second portion of TLF at operating point NS. The flows in the first portion determine the initial location and the direction of the interface, while the second portion determines the location of the interface's arrival onto the suction side. Both portion of TLF play important roles in determining whether the spillage happens or not.
3. The CFD simulations discover that the measured unsteady characteristics, namely the STD contours and the frequency spectra, can be explained with the self-induced unsteadiness of TLF. It is also found that the impingement of the second portion of the TLF is the one responsible for creating low-pressure spots on the pressure side of the neighboring blade, which is the key to originate the self-induced unsteadiness.

The above findings may offer a supporting idea to reexamine the effectiveness of the existing technologies to improve stall margin. With a clear sense of tip leakage flow structure and its evolution to unsteady status, its interface with the main flow could be controlled much before its spillover. The two ways for stability enhancement, either of existing techniques or currently under research, both may take the advantage of new findings. One is to change the structures of TLF with structural design or steady inputs and the other is to alter the unsteady dynamics between TLF and incoming main flow with unsteady excitations. More research efforts are anticipated in the near future.

Acknowledgment

This work was supported by National Basic Research Program 2007CB210104 of China, National Natural Science Foundation of China with project No. 51010007 and No. 51106153. These supports are gratefully acknowledged. The authors are very grateful to Professor Hongwu Zhang for his consistent support and valuable discussions.

Nomenclature

- P = static pressure (Pa)
- \bar{P} = time-averaged static pressure (Pa)
- P_{rt} = total pressure in the relative frame (Pa)
- P_{r0} = total pressure at inlet (Pa)
- π_{sp} = dimensionless static pressure normalized by the total pressure at inlet, $\Pi_{sp} = P/P_{r0}$
- C_p = static pressure coefficient, $C_p = (P - P_{r0})/(0.5\rho U_{tip}^2)$
- C_{rtip} = relative total pressure coefficient, $C_{rtip} = (P_{rt} - P_{r0})/(0.5\rho U_{tip}^2)$
- U_{tip} = corrected tip speed (m/s)
- σ = standard deviation of static pressure,
- $$\sigma = \sqrt{\frac{1}{N-1} \sum_{i=1}^N (P_i - \bar{P})^2}$$
- A = amplitude
- f = frequency normalized by blade passing frequency
- T = rotor blade passing period (s)
- C = blade tip chord
- Cva = axial velocity normalized by corrected tip speed
- Re_Mach = relative Mach number

Abbreviations

- TLF = tip leakage flow
BPF = blade passing frequency
STD = standard deviation
LE = leading edge
TE = trailing edge
PS = pressure side
SS = suction side
PE = operating points near peak efficiency
NS = operating points near stall

References

- [1] Denton, J. D., 1993, "Loss Mechanisms in Turbomachines," *ASME J. Turbomach.*, **115**, pp. 621–656.
- [2] Vo, H. D., Tan, C. S., and Greitzer, E. M., 2008, "Criteria for Spike Initiated Stall," *ASME J. Turbomach.*, **130**(1), p. 011023.
- [3] Lin, F., Zhang, J. X., Chen, J. Y., and Nie, C. Q., 2008, "Flow Structure of Short Length Scale Disturbance in an Axial Flow Compressor," *AIAA J. Propul. Power*, **24**(6), pp. 1301–1308.
- [4] Taharaf, N., Nakajiman, T., Kurosaki, M., Ohta, Y., Outa, E., and Nishikawa, T., 2001, "Active Stall Control With Practicable Stall Prediction System Using Auto-Correlation Coefficient," AIAA Paper No. 2001–3623.
- [5] Tong, Z. T., Lin, F., Chen, J. Y., and Nie, C. Q., 2007, "The Self-Induced Unsteadiness of Tip Leakage Vortex and its Effect on Compressor Stall Inception," *ASME* Paper No. GT2007-27010.
- [6] Lu, X. G., Zhu, J. Q., Nie, C. Q., and Huang, W. G., 2008, "The Stability-Limiting Flow Mechanism in a Subsonic Axial-Flow Compressor and Its Passive Control With Casing Treatment," *ASME* Paper No. GT2008-50006.
- [7] Muller, M. W., Schiffer, H., and Hah, C., 2007, "Effect of Circumferential Grooves on the Aerodynamic Performance of an Axial Single-Stage Transonic Compressor," *ASME* Paper No. GT2007-27365.
- [8] Bergner, J., Kinzel, M., Schiffer, H., and Hah, C., 2006, "Short Length-Scale Rotating Inception in a Transonic Axial Compressor-Experimental Investigation," *ASME* Paper No. GT2006-90209.
- [9] Biela, C., Muller, M. W., Schiffer, H., and Zschep, C., 2008, "Unsteady Pressure Measurement in a Single Stage Axial Transonic Compressor Near the Stability Limit," *ASME* Paper No. GT2008-50245.
- [10] Hah, C., Bergner, J., and Schiffer, H., 2006, "Short Length-Scale Rotating Stall Inception in a Transonic Axial Compressor-Criteria and Mechanisms," *ASME* Paper No. GT2006-90045.
- [11] Hah, C., Bergner, J., and Schiffer, H., 2008, "Tip Clearance Vortex Oscillation, Vortex Shedding and Rotating Instabilities in an Axial Transonic Compressor Rotor," *ASME* Paper No. GT2008-50105.
- [12] Adamczyk, J. J., Celestina, M. L., and Greitzer, E. M., 1993, "The Role of Tip Clearance in High-Speed Fan Stall," *ASME J. Turbomach.*, **115**, pp. 28–39.
- [13] Puterbaugh, S. L., and Brendel, M., 1997, "Tip Clearance Flow-Shock Interaction in a Transonic Compressor Rotor," *J. Propul. Power*, **13**(1), pp. 17–23.
- [14] Du, J., Lin, F., Zhang, H. W., and Chen, J. Y., 2010, "Numerical Investigation on the Self-Induced Unsteadiness in Tip Leakage Flow for a Transonic Fan Rotor," *ASME J. Turbomach.*, **132**(2), p. 021017.
- [15] Schulze, G., Blaha, C., Hennecke, D., and Henne, J., 1995, "The Performance of a New Axial Single Stage Transonic Compressor," Proceedings of the 12th ISABE, Melbourne, Australia, March 20–23, Paper No. ISABE-95-7072.
- [16] Bergner, J., and Hennecke, D. K., 2003, "Experimental Study of Stall Inception of a Single-Stage Transonic Compressor," Proceedings of the 16th Symposium Air Breathing Engines, Cleveland, OH, August 31–September 5, Paper No. ISABE-2003-1081.
- [17] Bennington, M. A., Cameron, J. D., Morris, S. C., and Gendrich, C. P., 2007, "Over Rotor Casing Surface Streak Measurements in a High Speed Axial Compressor," *ASME* GT2007-28273.
- [18] Inoue, M., and Kuromaru, M., 1989, "Structure of Tip Clearance Flow in an Isolated Axial Compressor Rotor," *ASME J. Turbomach.*, **111**, pp. 250–256.
- [19] Geng, S. J., 2007, "Numerical Study on the Unsteady Response of Compressor Tip Leakage Flow to Discrete Micro Tip Injection and Its Effect on Stability Enhancement," Ph.D. thesis, Graduate University of Chinese Academy of Sciences, Beijing, China.